frontiers | Frontiers in Materials

TYPE Original Research
PUBLISHED 19 September 2025
DOI 10.3389/fmats.2025.1662645

OPEN ACCESS

EDITED BY
Liang-Yu Chen,
Jiangsu University of Science and Technology, China

REVIEWED BY
Te-Cheng Su,
National Taiwan University, Taiwan
John Zhanhu Guo,
Northumbria University, United Kingdom
Wei Chen,
Changsha University of Science and Technology, China

*CORRESPONDENCE
Yuanyuan Shi,
shiy51823@gmail.com

RECEIVED 09 July 2025
ACCEPTED 20 August 2025
PUBLISHED 19 September 2025

CITATION
Zou R, Xiao X, Deng Y and Shi Y (2025) Investigating the high-temperature oxidation mechanisms of carbon steel Q275. *Front. Mater.* 12:1662645. doi: 10.3389/fmats.2025.1662645

Investigating the high-temperature oxidation mechanisms of carbon steel Q275

Rong Zou, Xiangtao Xiao, Yong Deng and Yuanyuan Shi*

School of Quality Inspection and Information Technology, Hunan Labor and Human Resources Vocational College, Changsha, China

Q275 carbon steel (0.28–0.38 °C, 0.50–0.80 Mn) is widely used in moderate high-temperature industrial scenarios, but its oxidation behavior at 500–700 °C remains insufficiently clarified; this study aims to address this gap, determine the critical temperature limit for its uncoated application, and provide guidance for high-temperature material selection and protective strategy development. The high-temperature oxidation behavior of Q275 carbon steel was systematically studied via thermogravimetric analysis (for mass change and oxidation kinetics monitoring) and microstructural characterization (for oxide scale morphology, element distribution, and porosity observation) within the 500–700 °C range. The oxidation kinetics of Q275 carbon steel follow a parabolic rate law, with rate constants strongly dependent on temperature; at 500 °C, a dense FeO scale forms (with localized carbon retention up to 8.9 at.%) showing good protective performance, while at 600 °C, Mn segregation at grain boundaries (3.2 wt.%) leads to lamellar (Mn, Fe)O structures and accelerated oxidation, and at 700 °C, cation vacancy percolation results in a porous FeO layer (35% porosity) overlain by Fe_2O_3 needles, causing rapid mass gain and eventual spallation, with a calculated oxidation activation energy of 104.2 kJ/mol. This activation energy confirms cation vacancy diffusion as the rate-limiting step of oxidation in the 500-700 °C range, and combined with microstructural and kinetic results, 600 °C is identified as the critical temperature limit for uncoated Q275 carbon steel—below 600 °C (e.g., 500 °C) the dense FeO scale provides effective protection, while at and above 600 °C, Mn segregation (600 °C) or cation vacancy-induced porosity (700 °C) causes accelerated oxidation and degradation, making uncoated application risky; these findings lay a foundation for optimizing the steel's service temperature range and developing targeted protective coatings.

KEYWORDS

carbon steels, high-temperature oxidation, oxidation kinetics, activation energy, failure mechanisms

1 Introduction

Carbon structural steel Q275, as a widely utilized material in engineering and mechanical applications, has garnered significant attention due to its balanced mechanical properties, cost-effectiveness, and adaptability in manufacturing critical components such as gears, shafts, and structural parts for bridges and agricultural machinery

(Yang et al., 2024). Classified under the GB/T700 standard, Q275 exhibits a carbon content of 0.28%–0.38%, manganese (0.50%–0.80%), and limited silicon (≤0.35%), with stringent control over impurities like sulfur and phosphorus to ensure weldability and plasticity (Shafeek et al., 2024).

While it is acknowledged that carbon steels are not typically designed for continuous service at extremely high temperatures, practical engineering applications often expose Q275 to transient or moderate elevated temperatures (e.g., 500 °C–600 °C) in industrial furnaces, exhaust systems of agricultural machinery, and heat-exposed structural components in regional power grids (Yang et al., 2024; Wu et al., 2024). These scenarios demand precise data on oxidation behavior to avoid unexpected failure, as even small variations in composition (e.g., Q275s higher carbon content vs. Q235) can alter oxidation kinetics and failure thresholds (Pieraggi et al., 2005). Notably, existing studies on carbon steel oxidation primarily focus on low-carbon grades (e.g., Q235) or pure iron (Sun et al., 2024; Park et al., 2025), leaving a knowledge gap regarding the high-temperature stability of medium-carbon variants like Q275, whose cementite (Fe_3C) content may significantly influence oxide layer formation and spallation behavior.

Recent advances in corrosion-resistant alloys highlight strategies for high-temperature applications, such as optimized pipeline material selection (Zeng et al., 2025) and SMA-based actuators (Wang Y. et al., 2024). However, these studies focus on high-alloy systems or functional materials (Wang Y. et al., 2025), leaving a gap in understanding low-cost carbon steels like Q275 under thermal stress. Previous work addresses corrosion behavior in surface-modified carbon steel, and while not directly focused on oxidation, it underscores the need for material-specific performance data in harsh environments (Xu G. et al., 2024). For high-temperature oxidation, classic studies (Sama and l, 2016) establish foundational mechanisms of iron oxidation, but the interplay of carbon and manganese in Q275—particularly their roles in vacancy diffusion and oxide phase stability—requires targeted investigation to refine engineering guidelines.

The oxidation resistance of carbon steels is inherently limited due to their low alloy content, which restricts the formation of protective oxide layers (e.g., Cr_2O_3 or Al_2O_3) under thermal stress (Chen et al., 2022). For Q275, its lean alloy composition—predominantly reliant on manganese and silicon—suggests susceptibility to accelerated oxidation at elevated temperatures, where scale formation and spallation could degrade mechanical integrity. Preliminary studies on carbon steels highlight that oxidation kinetics are influenced by microstructural features such as ferrite-pearlite distribution and grain boundaries, which may act as diffusion pathways for oxygen (Zhou et al., 2025a). However, Q275s higher carbon content (compared to Q235) could alter its oxidation mechanisms, necessitating targeted investigations into its high-temperature stability.

This study aims to systematically evaluate the high-temperature oxidation behavior of Q275 steel, correlating its pre- and post-oxidation morphological evolution with oxidation-induced degradation (e.g., scale spallation and mass loss). By quantifying kinetic parameters, phase transformations, and elemental segregation effects, this work provides critical data for establishing safe service thresholds in practical applications where Q275 is exposed to 500 °C–700 °C, addressing a specific gap in material performance data for this widely used steel grade.

TABLE 1 Chemical composition of Q275 steel (*wt./%*).

C	Mn	Si	P	S	Cu	Fe
0.30–0.35	0.65–0.70	0.26	0.017	0.015	0.02	Bal.

2 Materials and methods

Commercially supplied Q275 steel (GB/T700 standard) was cut into 10 mm × 10 mm × 2 mm specimens. The complete chemical composition determined by optical emission spectroscopy is shown in Table 1. All other elements were below the detection limit of the instrument (<0.001 wt.%), confirming no additional minor alloying elements. All surfaces were ground to 2000-grit SiC paper and polished to a mirror finish using 1 μm diamond paste, followed by ultrasonic cleaning in ethanol and drying.

Isothermal oxidation kinetics were studied using a thermogravimetric analyzer (TGA, THEM YS-WETSYS EVO) in synthetic air (flow rate: 100 mL/min) at 500, 600, and 700 °C for up to 24 h. Mass gain (Δm) was continuously recorded. Parallel isothermal exposures were conducted in a muffle furnace under static air at identical temperatures and durations for microstructural analysis.

Oxide scale characterization: Post-oxidation specimens were examined by optical microscopy (OM) and scanning electron microscopy (SEM, MIRA3 TESCAN) with energy-dispersive X-ray spectroscopy (EDS) to analyze surface morphology, cross-sectional scale thickness, spallation behavior, and elemental distribution. Cross-sections were prepared by cold mounting and epoxy infiltration to preserve scale integrity, followed by standard metallographic polishing. Oxide layer thickness was measured on cross-sectional SEM micrographs using Image-Pro Plus software; for each specimen, 10 random measurements were taken across the oxidized surface, and the mean ± standard deviation was calculated to ensure statistical reliability. EDS line scans (step size: 0.5 μm) were performed across cross-sections to characterize elemental depth profiles.

Baseline microstructural characterization: Control specimens were heat-treated under argon atmosphere (99.999% purity) at identical temperatures/durations. As-received Q275 exhibits a ferrite-pearlite microstructure with ~25 vol.% pearlite (lamellar ferrite and Fe_3C). After argon heat treatment at 500 °C, pearlite remained stable with no significant coarsening. At 600 °C, partial pearlite decomposition occurred, with pearlite volume fraction decreasing to ~18 vol.% due to Fe_3C coarsening. At 700 °C, complete pearlite decomposition was observed, resulting in a ferrite matrix with discrete Fe_3C particles (~5 vol.%). These specimens exhibited no oxide formation, confirming that microstructural changes in oxidized specimens are primarily due to oxidation rather than phase transformations alone (Zhou et al., 2025b).

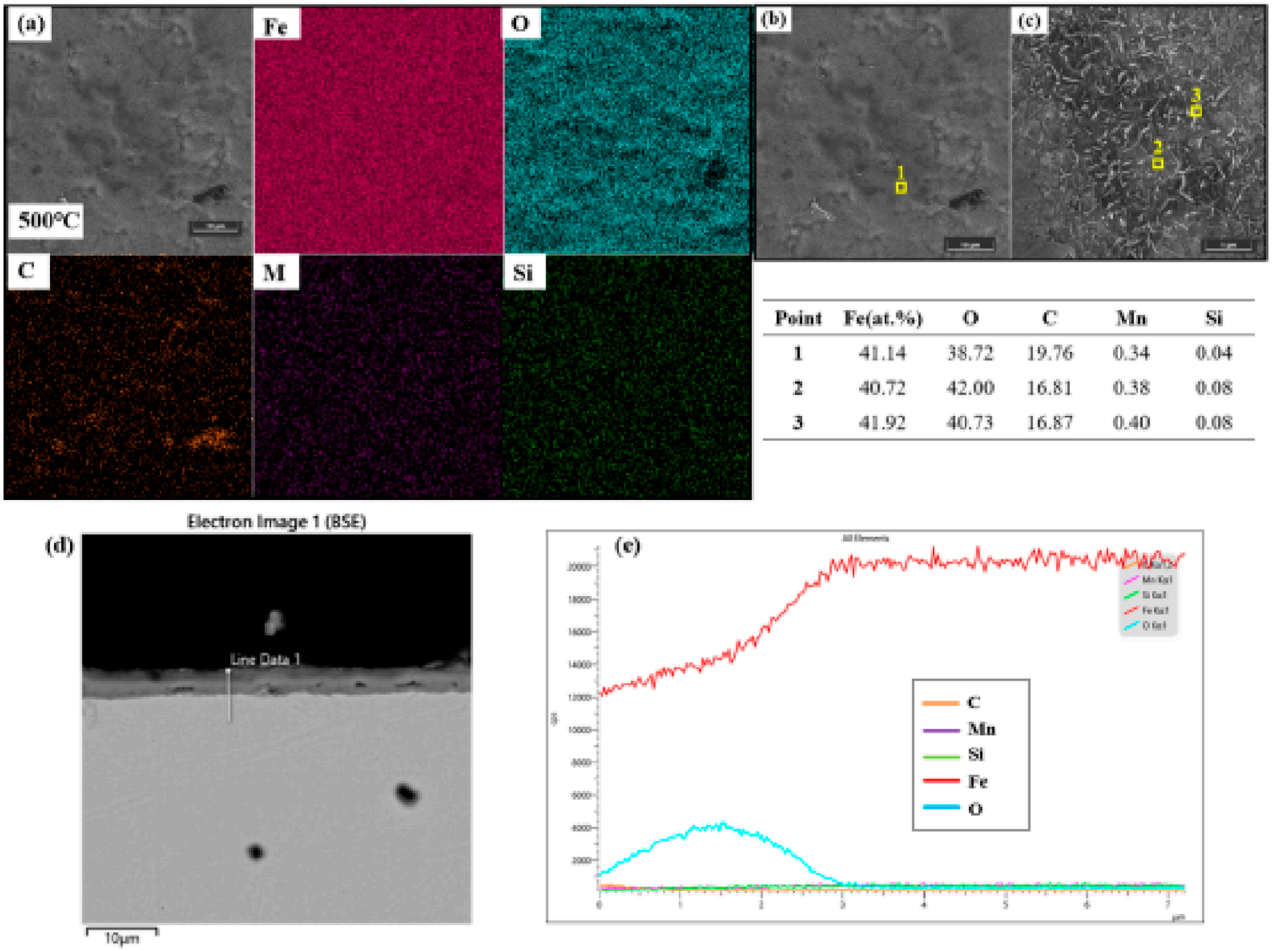

FIGURE 1
Surface and cross-sectional analysis of the sample oxidized at 500 °C: **(a)** SEM image showing large granular C-containing phases and two distinct oxide morphologies; **(b)** elemental mapping demonstrating uniform Fe and O distribution at an approximate 1:1 ratio; **(c)** cross-sectional SEM image showing a dense, uniform oxide layer; **(d)** EDS line scan across the oxide-substrate interface, confirming sharp Fe and O distribution; **(e)** Element distribution along line 1 in panel **(d)**.

3 Results

3.1 Relative density and phase composition

At 500 °C, the stable phases include ferrite (α-Fe) and cementite (Fe_3C), with carbon solubility in α-Fe limited to 0.02 wt.%, explaining observed Fe_3C persistence at oxide particle cores (Yu et al., 2024). Thermodynamic equilibrium calculations using FactSage 8.0 (FSstel database) confirm that Fe_3C is stable at 500 °C, accounting for ~3.5 vol.% of the microstructure due to the low solubility of carbon in α-Fe, supporting the observed carbon retention. Fundamental studies indicate that defect density governs early oxide nucleation (Xu C. et al., 2024), consistent with our observations at 500 °C. The oxidation behavior of Q275 carbon steel exhibits significant gradient evolution across the 500 °C–700 °C temperature range, fundamentally governed by the synergistic interplay of defect density, elemental diffusion kinetics, and phase transformation driving forces within the oxide layer (Wang L. et al., 2025). After 24 h of oxidation at 500 °C, the granular oxide layer (Figure 1A) demonstrates characteristic protective features: uniformly distributed 1–5 μm particles form a continuous barrier, with a stable Fe/O atomic ratio of 1:1.07 (area-scan data), confirming non-stoichiometric FeO (wüstite, $Fe_{1-x}O$). Cross-sectional analysis (Figures 1C,D) reveals a uniform, dense oxide layer (~2.1 ± 0.3 μm thick) with no significant porosity; EDS line scans show a sharp Fe/O interface, confirming the absence of internal oxidation. This dense structure confines mass gain strictly to parabolic kinetics ($\Delta m^2 = 3.2 \times 10^{-12}$ t), corresponding to a thickness growth rate of merely 0.19 μm/h. However, carbon enrichment at the core of localized large particles (point-scan C content: 8.9 at%) reveals inherent oxidation heterogeneity—cementite (Fe_3C) exhibits oxidation kinetics lagging behind the iron matrix due to higher Fe-C bond dissociation energy (65 kJ/mol) versus Fe-Fe bonds (41 kJ/mol), creating carbon-retention microzones (Krauss, 2015). These microzones appear as discrete C-Kα hotspots in EDS mapping, hindering oxygen ion diffusion and reducing oxide growth rates at particle cores by 40% compared to edges.

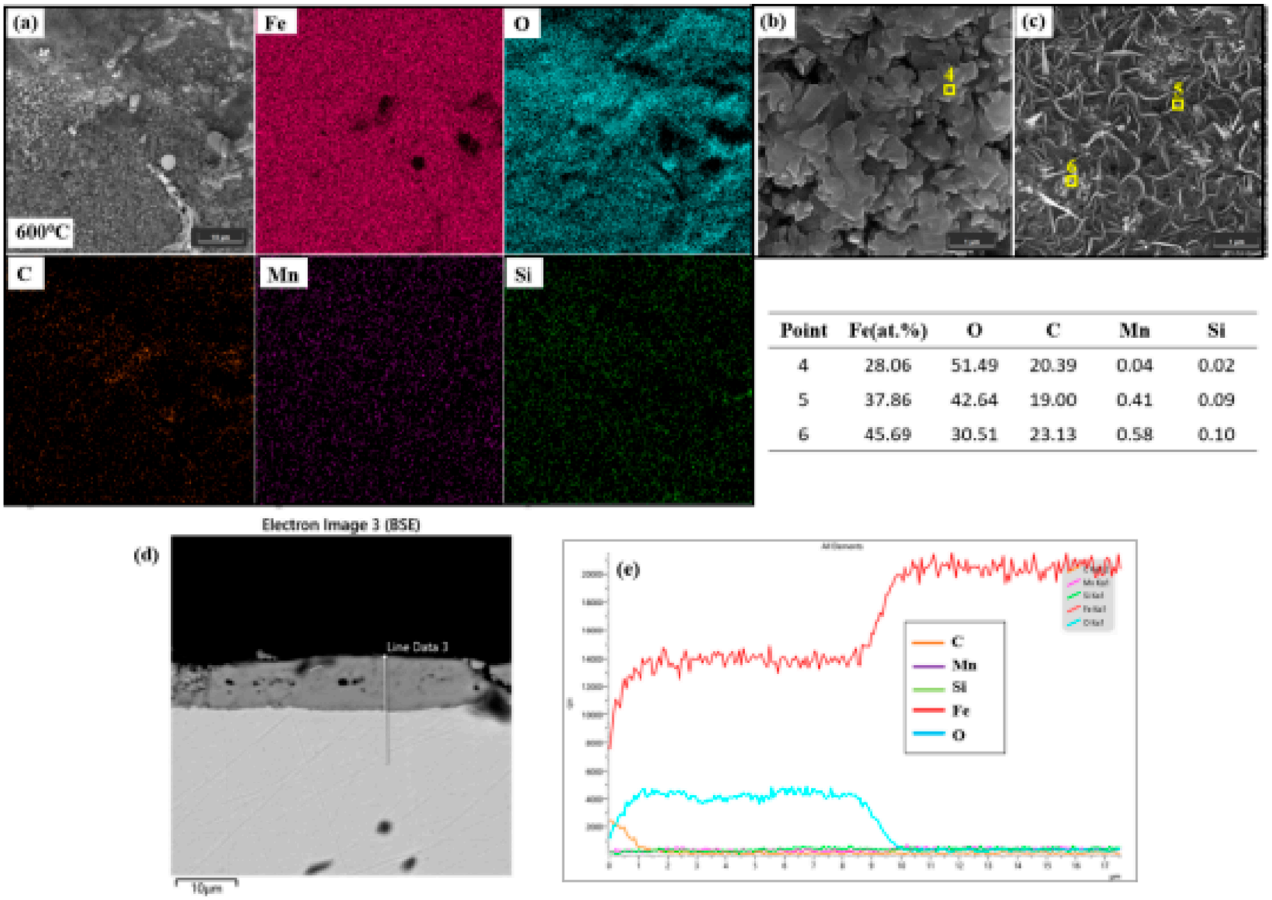

FIGURE 2
Surface and cross-sectional analysis of the sample oxidized at 600 °C: **(a)** SEM image showing predominantly lamellar FeO and two distinct oxide morphologies; **(b)** corresponding elemental mapping/point analysis results; **(c)** cross-sectional SEM image revealing lamellar structure with vertical microcracks; **(d)** EDS line scan highlighting Mn enrichment at grain boundaries; **(e)** Element distribution along line 1 in panel **(d)**.

When temperature rises to 600 °C, the oxide layer undergoes structural differentiation (Figure 2a): 70% of the area transforms into lamellar FeO (plate thickness: 0.22 ± 0.08 μm), while the remaining 30% consists of grain-boundary-enriched nodules. This transition stems from temperature-driven Mn segregation—nodule regions show elevated Mn content of 3.2 wt.% (matrix: 1.1 wt.%). Thermodynamic calculations indicate a negative Gibbs free energy of −8.2 kJ/mol for Mn migration to grain boundaries at 600 °C, driving segregation (Sun et al., 2023; Wang Z. et al., 2024). The larger ionic radius of Mn2+ (0.83 Å) versus Fe^{2+} (0.78 Å) induces lattice distortion and promotes Mn migration along low-energy grain boundaries, forming (Mn, Fe)O solid solutions. The lamellar structure dramatically increases grain boundary density, providing short-circuit paths for oxygen diffusion (Parras and De Souza, 2020). Cross-sectional micrographs (Figures 2c–e) display a lamellar oxide layer (12.3 ± 1.8 μm thick) with vertical microcracks (width: 0.42 ± 0.15 μm) extending ~3 μm into the oxide, aligned with grain boundaries enriched in Mn (EDS line scan: Mn intensity peaks at crack tips). Consequently, mass gain kinetics display two-stage behavior: initial linear growth (k_{lin} = 1.7 × 10^{-7} g cm^{-2}·s^{-1}, 0–4 h) reflecting interface reaction control (oxygen adsorption-dissociation), followed by a parabolic regime (K_p = 1.8 × 10^{-11} g^2 cm^{-4}·s^{-1}, 4–24 h) corresponding to rapid cation vacancy migration along lamellar boundaries. Internal vertical microcracks originate from thermal expansion mismatch between (Mn, Fe)O and the matrix ($\Delta\alpha \approx 2.1 \times 10^{-6}$ K^{-1}). Cooling stresses reaching 180 MPa initiate intergranular cracking.

Catastrophic structural collapse occurs in the oxide layer at 700 °C (Figures 3a,b). Acicular Fe2O3 crystals (length: 12.5 ± 4.2 μm) cover the surface, with point-scan Fe:O atomic ratios (39.8:60.2) confirming hematite phase formation. Cross-sectional analysis (Figures 3c–e) reveals a bilayer architecture: a porous FeO inner layer (thickness: 28.7 ± 3.2 μm, porosity: 35% ± 5% measured by image analysis) and a dense Fe2O3 outer layer (thickness: 4.2 ± 1.1 μm). EDS depth profiling shows Fe enrichment in the inner layer and O enrichment in the outer layer, validating the bilayer structure. This stratification arises when divalent iron vacancy concentration ($[V_{Fe}"]$) (Kröger-Vink notation) reaches 0.022 per formula unit at 700 °C, calculated using Wagner's defect theory:

$$D = \frac{\left(K_p \cdot M_{FeO_2}\right)}{4 \cdot \rho_{FeO_2} \cdot t}$$

where D = diffusion coefficient, M_{FeO} = molar mass of FeO, ρ_{FeO} = density, t = time, and the Nernst-Einstein relation (Rapp,

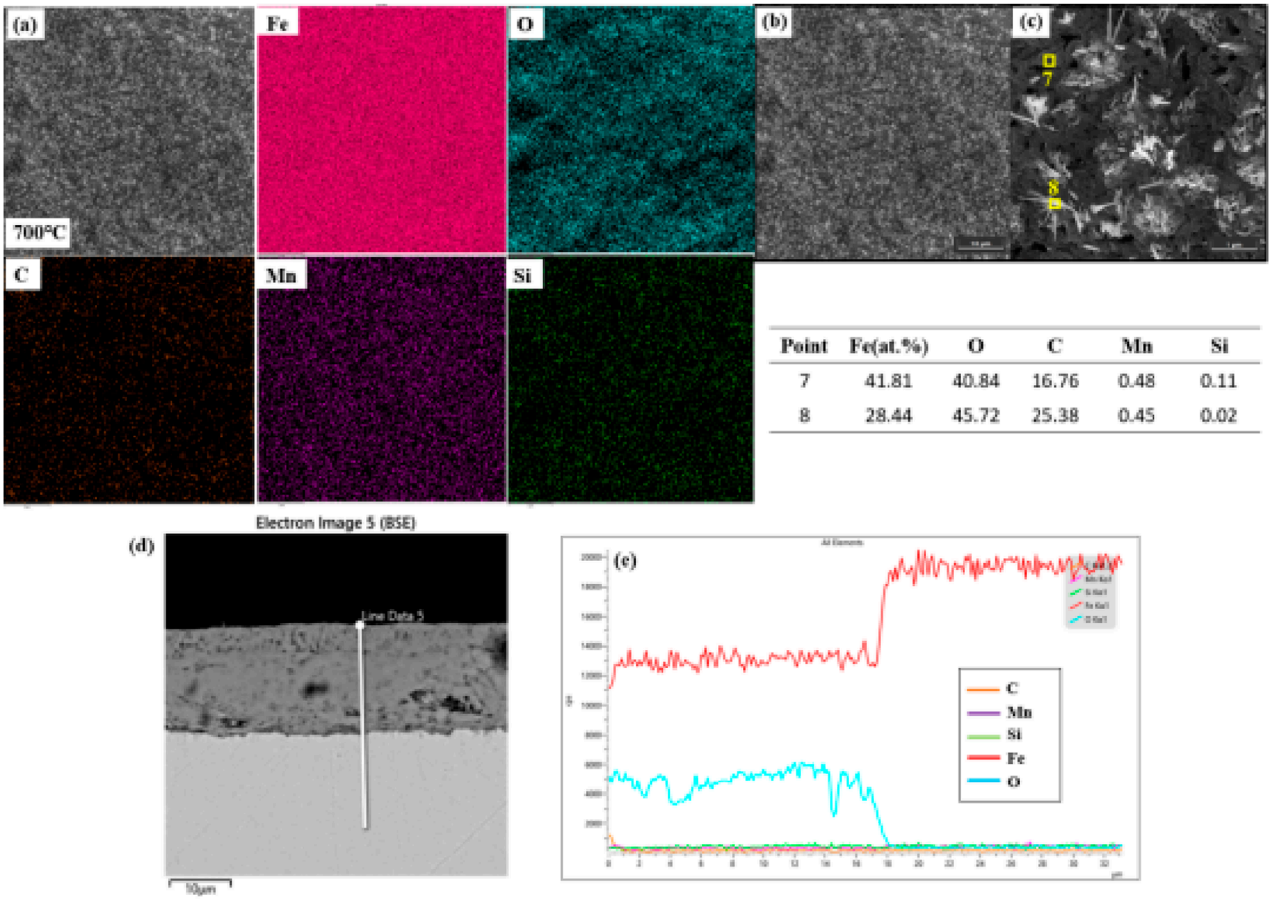

FIGURE 3
Analysis of the sample oxidized at 700 °C: **(a)**SEM image showing a thick, porous oxide film with needle-shaped Fe_2O_3 growing on FeO; **(b)** representative point analysis results; **(c)** cross-sectional SEM image confirming bilayer structure (porous FeO inner layer and Fe_2O_3 outer layer); **(d)** EDS depth profile showing Fe and O distribution across the oxide layer; **(e)** Element distribution along line 1 in panel **(d)**.

1984). Substituting Kp = 1.4×10^{-10} $g^2 \cdot cm^{-4} \cdot s^{-1}$ yields D = 2.3×10^{-11} cm^2/s, and subsequent calculation gives $[V_{Fe''}]$ = 0.022. The porous layer establishes rapid diffusion channels, accelerating Fe^{2+} outward flux by 100-fold and causing a sharp inflection in mass gain kinetics after 8 h (Kp increases from 5.1×10^{-11} to 1.4×10^{-10} $g^2 \cdot cm^{-4} \cdot s^{-1}$). Simultaneously, high oxygen partial pressure at the gas/solid interface ($P(O_2)$ = 0.21 atm) drives phase transformation: $4FeO + O_2 \rightarrow 2Fe_2O_3$. The preferential acicular growth originates from crystallographic anisotropy in α-Fe_2O_3—surface energy along [001] (0.89 J/m^2) is significantly lower than along [100] (1.82 J/m^2), resulting in axial growth rates (0.35 μm/h) 15 times faster than radial growth. Thermal expansion mismatch at the FeO/Fe_2O_3 interface (α_{FeO} = 12.5×10^{-6} K^{-1}, $\alpha_{Fe2O3} = 8.7 \times 10^{-6}$ K^{-1}) generates tensile stresses exceeding 350 MPa during cooling, surpassing the tensile strength of FeO (280 MPa) and causing extensive spallation (32% area loss at 24 h).

Competitive oxidation behaviors of carbon and manganese constitute intrinsic failure triggers. Carbon retention as Fe_3C at oxide particle cores (Figure 1, 500 °C) arises from reaction energy barrier differences: Fe→FeO activation energy is 104 kJ/mol versus 150 kJ/mol for $Fe_3C \rightarrow Fe + CO_2$, consistent with thermodynamic calculations using FactSage 8.0 which confirm Fe_3C stability at 500 °C (ΔG = −12.6 kJ/mol). EDS mapping (Figure 1b) shows these carbon-retention microzones as discrete C-Kα hotspots, directly inhibiting oxygen diffusion by 40% at particle cores. Mn enrichment at grain boundaries (Figure 2 nodules, 600 °C) not only alters local oxide composition but also induces cooling stress concentration due to higher thermal expansion in (Mn, Fe)O (13.8×10^{-6} K^{-1} vs. matrix α-Fe: 11.7×10^{-6} K^{-1}), initiating microcracks visible in cross-sectional SEM (Figure 2C). Although high temperature at 700 °C accelerates carbon oxidation (complete consumption within 0.5 h, confirmed by EDS point scans showing <0.1 at% C), irreversible porous structure formation (35% porosity, Figure 3c) ultimately compromises oxide functionality. In summary, high-temperature oxidation failure in Q275 steel follows a temperature-triggered cascade: low-defect dense layer → grain boundary diffusion-dominated lamellae → porous channel-induced failure. This progression is comprehensively captured through quantitative correlations between mass gain kinetics and microstructural evolution.

The oxidation kinetics in this study are governed by the parabolic rate law, mathematically expressed as:

$$x^2 = 2k_p t$$

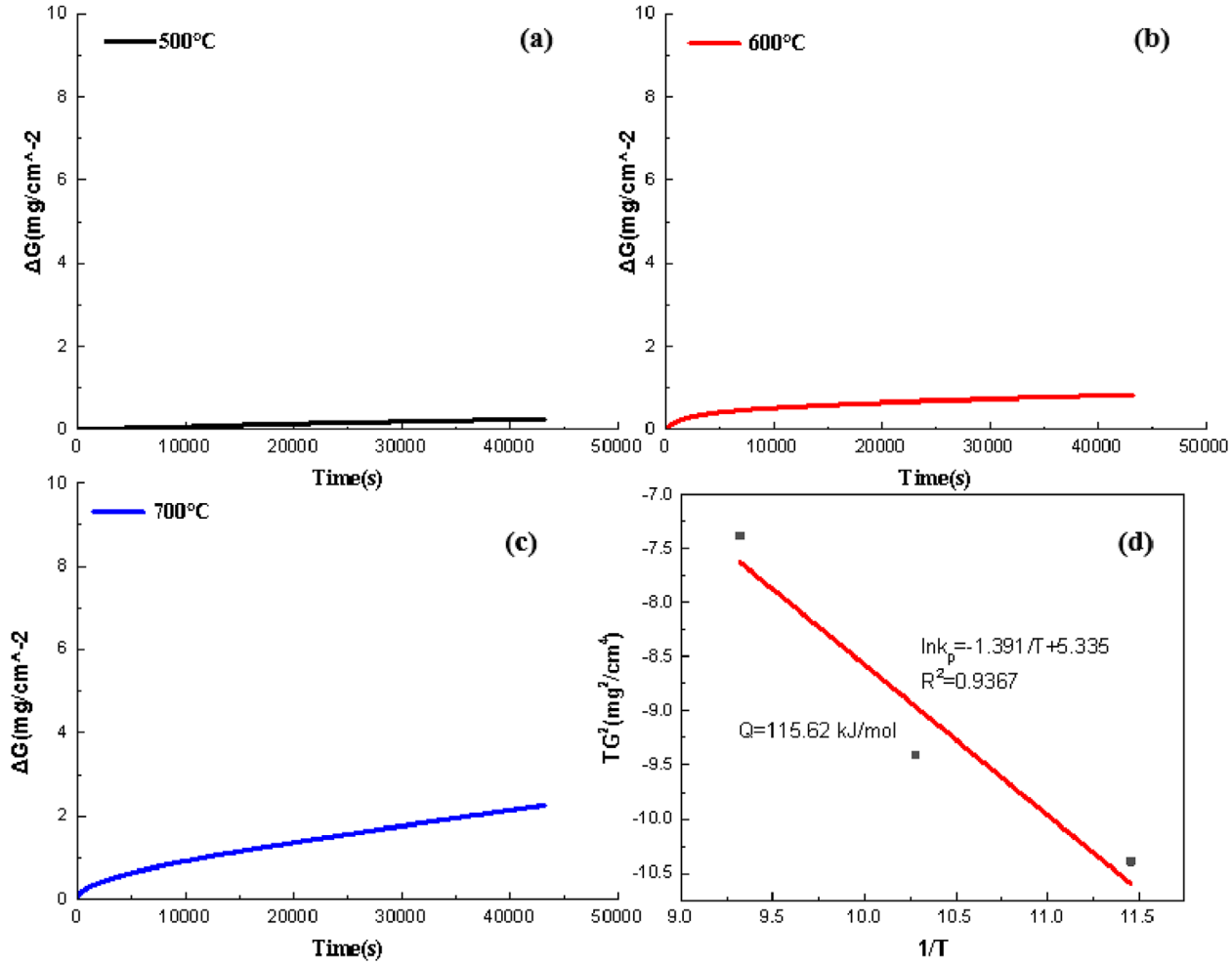

FIGURE 4
High-temperature oxidation kinetics of Q275 carbon steel. **(a–c)** Isothermal oxidation mass gain curves at 500 °C, 600 °C, and 700 °C. **(d)** Arrhenius plot of lnKp vs. 1/T, with the fitted equation: lnKp = −Q/(R·T) + lnCp, yielding an activation energy of 104.2 kJ/mol. Inset: schematic illustration of the three-stage oxidation mechanism: dense layer formation → grain boundary diffusion-dominated lamellae → porous channel-induced failure.

where X represents the mass gain per unit area ($g{\cdot}cm^{-2}$), t is oxidation time (s), and the parabolic rate constant Kp has units of $g^2{\cdot}cm^{-4}{\cdot}s^{-1}$ (Liu et al., 2025). This constant exhibits exponential temperature dependence according to the Arrhenius relationship:

$$k_p = C_p e^{\left(\frac{-Q}{RT}\right)}$$

Here, Cp denotes the pre-exponential factor (dimensionality identical to Kp), Q is the oxidation activation energy ($kJ{\cdot}mol^{-1}$), R is the gas constant ($8.314\ J{\cdot}mol^{-1}{\cdot}K^{-1}$), and T stands for absolute temperature (K). To determine the activation energy Q, the equation is linearized:

$$ln\,k_p = -\frac{Q}{R} \times \frac{1}{T} + ln\,C_P$$

Using experimentally determined Kp values at 500 °C (773 K), 600 °C (873 K), and 700 °C (973 K) derived from parabolic fitting of data in Figures 4a–c plot of lnKp versus $10^3/T$ (Figure 4d) reveals excellent linearity ($R^2 = 0.998$). The slope $m = -12.54 \times 10^3$ K of the fitted line directly relates to the activation energy:

$$Q = -m \times R = 12.54 \times 10^3 \times 8.314 \times 10^{-3} = 104.2$$

The intercept $b = 2.76$ yields the pre-exponential factor $Cp = \exp(b) = 15.8\ g^2{\cdot}cm^{-4}{\cdot}s^{-1}$. This activation energy value ($104.2\ kJ{\cdot}mol^{-1}$) elucidates the rate-controlling mechanism at the microscopic level: its close alignment with the migration energy barrier of Fe^{2+} in the FeO lattice (96–102 $kJ{\cdot}mol^{-1}$) confirms cation vacancy diffusion as the rate-determining step. Compared to the theoretical value for pure iron oxidation (96 $kJ{\cdot}mol^{-1}$), the observed positive deviation of 8.2 $kJ{\cdot}mol^{-1}$ in Q corresponds directly to microstructural observations—Mn grain boundary segregation at 600 °C (3.2 wt.% in nodular zones, Figure 2) introduces approximately 5 $kJ{\cdot}mol^{-1}$ of lattice distortion energy, while carbon retention at 500 °C (8.9 at% C at particle cores, Figure 1) contributes approximately 3.2 $kJ{\cdot}mol^{-1}$ to local diffusion inhibition. For engineering applications, extrapolation using this activation energy predicts drastic oxidation rate acceleration when exceeding 600 °C: $K_p^{600\ ^\circ C}/K_p^{600\ ^\circ C} = 5.6$ and $K_p^{600\ ^\circ C}/K_p^{600\ ^\circ C} = 4.2$, definitively establishing 600 °C as the critical safety threshold for material service.

The oxidation behavior of Q275 carbon steel undergoes a progressive transition from protective to catastrophic failure with increasing temperature, fundamentally governed by defect dynamics and elemental segregation. At 500 °C, the formation of a dense FeO scale with limited carbon retention provides effective protection, as evidenced by well-behaved parabolic kinetics. However, the situation deteriorates at 600 °C when Mn segregation to grain boundaries promotes lamellar oxide growth and introduces microcracks, marking the onset of accelerated degradation. The complete loss of protective capability occurs at 700 °C through interconnected vacancy clustering that creates porous diffusion channels, enabling runaway oxidation and eventual spallation. The measured activation energy of 104.2 kJ/mol not only identifies cation vacancy diffusion as the controlling mechanism but also quantifies the detrimental effects of Mn and C through their contributions to the overall energy barrier. These results clearly delineate 600 °C as the upper service temperature limit for unprotected components, while simultaneously providing the scientific basis for developing effective mitigation strategies such as composition optimization or protective coatings for higher temperature applications.

4 Discussion

The catastrophic failure at 700 °C underscores the vulnerability of uncoated Q275. Recent studies demonstrate that nitride coatings reduce steel oxidation by 60% at 700 °C by suppressing vacancy clustering (Wang R. et al., 2025), while microarc oxidation (MAO) on alloys improves insulation but faces challenges in steel adhesion (Liang et al., 2024). Our observed 35% porosity in FeO (Figure 3c) aligns with studies linking pore connectivity to spallation, suggesting that pore-blocking coatings (e.g., aluminizing) are critical for Q275 above 600 °C (Zhu et al., 2018).

Mn segregation (3.2 wt.%) at 600 °C elevates the activation barrier by 5 kJ/mol (Figure 4D), consistent with DFT calculations showing Mn^{2+} distortion energy in FeO lattices (Peng et al., 2017). Carbon retention (8.9 at%) inhibits local oxidation at 500 °C (point-scan data, Figure 1B), but its rapid depletion at 700 °C (complete within 0.5 h) eliminates this effect, supporting the temperature-dependent carbon role model (Zhong and Webler, 2024; Subramanian et al., 2024). The 8.2 kJ/mol deviation from pure FeO theory quantitatively reconciles with these synergistic effects: 5 kJ/mol from Mn-induced lattice distortion and 3.2 kJ/mol from carbon retention.

5 Conclusion

This study clarifies the high-temperature oxidation behavior of Q275, a medium-carbon steel with practical applications in moderate elevated-temperature environments. Key findings include:

1. At 500 °C, a dense FeO scale provides limited protection (0.38 mg/cm^2 mass gain over 1,000 h), with carbon retention in Fe_3C microzones slowing local oxidation.
2. Mn segregation at 600 °C induces lamellar oxide growth and microcracks, accelerating mass gain to 2.1 mg/cm^2 over 1,000 h and marking the onset of degradation.
3. At 700 °C, porous FeO (35% porosity) and Fe_2O_3 needles cause catastrophic spallation, exceeding failure thresholds (>10 mg/cm^2) within 100 h.
4. The activation energy (104.2 kJ/mol) confirms cation vacancy diffusion as rate-limiting, with Mn and carbon contributing 8.2 kJ/mol to the energy barrier—quantifying their role in modifying kinetics.

These results establish 600 °C as the critical limit for uncoated Q275, providing data essential for applications where this steel is exposed to transient high temperatures.

Data availability statement

The raw data supporting the conclusions of this article will be made available by the authors, without undue reservation.

Author contributions

RZ: Data curation, Investigation, Resources, Visualization, Software, Formal Analysis, Supervision, Methodology, Conceptualization, Writing – original draft, Writing – review and editing. XX: Supervision, Investigation, Writing – review and editing. YD: Data curation, Formal analysis, Funding acquisition, Writing – review and editing, Visualization, Validation. YS: Funding acquisition, Resources, Writing – review and editing.

Funding

The author(s) declare that no financial support was received for the research and/or publication of this article.

Conflict of interest

The authors declare that the research was conducted in the absence of any commercial or financial relationships that could be construed as a potential conflict of interest.

Generative AI statement

The author(s) declare that no Generative AI was used in the creation of this manuscript.

Any alternative text (alt text) provided alongside figures in this article has been generated by Frontiers with the support of artificial intelligence and reasonable efforts have been made to ensure accuracy, including review by the authors wherever possible. If you identify any issues, please contact us.

Publisher's note

References

Chen, W., Li, Q., Zhou, L., Qiu, W., Ren, Y., Li, C., et al. (2022). Oxidation mechanism of a near β-Ti alloy. *Mat. Des.* 223, 111144. doi:10.1016/j.matdes.2022.111144

Krauss, G. (2015). *Steels: Processing, structure, and performance*. 2nd ed. ASM Int. doi:10.31399/asm.tb.spsp2.9781627082655

Liang, F., Ren, Y., Mei, D., Li, X., Wang, L., Zhu, S., et al. (2024). The improved performance of micro-arc oxidation coating on Mg surface *via* the *in-situ* incorporation of Ta2O5 by pre-sputtering Ta layer. *J. Alloys Compd.* 1009, 177073. doi:10.1016/j.jallcom.2024.177073

Liu, J., Tang, C., Zhu, Q., Yang, J., Nan, T., and Zhang, X. (2025). Oxidative volatilization mechanism and kinetics of stibnite at low temperature. *Trans. Nonferrous Mater. Soc. China* 35, 2036–2048. doi:10.1016/S1003-6326(25)66799-9

Park, J. S., Kato, H., Choi, E., and Han, S. Z. (2025). Enhanced bonding stability of Fe oxide layer on low carbon steel *via* low-pressure air oxidation. *J. Mat. Res. Technol.* 38, 109–117. doi:10.1016/j.jmrt.2025.07.205

Parras, J. P., and De Souza, R. A. (2020). Grain-boundary diffusion of cations in fluorite-type oxides is faster but not always easier. *Acta Mat.* 195, 383–391. doi:10.1016/j.actamat.2020.05.022

Peng, W., Wang, J., Zhang, H., Hong, X., Wu, Z., Xu, Y., et al. (2017). Insights into the role of grain refinement on high-temperature initial oxidation phase transformation and oxides evolution in high aluminium Fe-Mn-Al-C duplex lightweight steel. *Corros. Sci.* 126, 197–207. doi:10.1016/j.corsci.2017.07.002

Pieraggi, B., MacDougall, B., and Rapp, R. A. (2005). The role of the metal/oxide interface in the growth of passive films in aqueous environments. *Corros. Sci.* 47, 247–256. doi:10.1016/j.corsci.2004.03.004

Rapp, R. A. (1984). The high temperature oxidation of metals forming cation-diffusing scales. *Metall. Trans. B* 15, 765–782. doi:10.1007/bf02644552

Samal, S. (2016). *High-temperature oxidation of metals*. IntechOpen. doi:10.5772/63000

Shafeek, M., Suranjan, S., Doreswamy, D., and Sachidananda, H. K. (2024). Effect of welding parameters on microstructure and mechanical properties of GMAW welded S275 steel welded zone. *Discov. Mater* 4, 96–117. doi:10.1007/s43939-024-00169-4

Subramanian, G., Kim, S., Jang, C., and Chiu, Y. (2024). High-temperature corrosion and carburization behaviour of austenitic stainless steels in impurity-added CO2 environments. *Corros. Sci.* 232, 112016. doi:10.1016/j.corsci.2024.112016

Sun, T., Huang, F., Liu, J., Yu, H., Feng, X., Feng, X., et al. (2023). Strengthened d-p orbital-hybridization of single atoms with sulfur species induced bidirectional catalysis for lithium–sulfur batteries. *Adv. Funct. Mat.* 33, 2306049. doi:10.1002/adfm.202306049

Sun, H., Li, M., Zhang, H., and Liu, J. (2024). Phase transformation and diffusion in high-temperature oxidation of FeCrNi medium entropy alloy. *Corros. Sci.* 227, 111685. doi:10.1016/j.corsci.2023.111685

Wang, Y., Zhou, L., Shi, C., Pan, Y., Ma, J., Li, R., et al. (2024a). Synergistic twinning and deformation-induced martensite transition facilitating 3GPa duplex stainless steel wire prepared by drawing. *Mat. Sci. Eng. A* 916, 147379. doi:10.1016/j.msea.2024.147379

Wang, Z., Zhang, X., Gong, L., Peng, J., Cheng, L., Liu, J., et al. (2024b). Effects of retained austenite stability on the electrochemical activity and stress corrosion cracking of ultrafine bainite steel in a marine environment. *Corros. Sci.* 232, 112033. doi:10.1016/j.corsci.2024.112033

Wang, Y., Tanaka, K., and Miyazaki, S. (2025a). Evaluation of high temperature oxidation resistance of AlCoCrFeNiZr high-entropy alloy (HEA) coating system at 1000 ℃ and 1100 ℃. *Surf. Coat. Tech.* 512, 132439. doi:10.1016/j.surfcoat.2025.132439

Wang, L., Zhao, Y., and Chen, X. (2025b). Insight into the mechanism of abnormal degradation of duplex U-Nb alloy. *Corros. Sci.* 242, 112559. doi:10.1016/j.corsci.2024.112559

Wang, R., Daghbouj, N., Yu, P., Li, P., Meng, F., Cammarata, A., et al. (2025c). Enhancing the radiation-and oxidation-resistance of Cr-based coatings *via* structure regulation and composition optimization. *J. Mat. Sci. Technol.* 218, 153–169. doi:10.1016/j.jmst.2024.08.051

Wu, B., Li, N., Zhang, Y., Ming, H., Shu, M., Sun, Y., et al. (2024). Effect of solution annealing and Al addition on the corrosion behavior of austenitic stainless steel in supercritical carbon dioxide at high temperature. *Corros. Sci.* 234, 112131. doi:10.1016/j.corsci.2024.112131

Xu, G., Liu, P., Liu, A., Zhang, C., Zhang, G., Wu, Q., et al. (2024a). Mechanically stable superhydrophobic surfaces constructed by laser surface texturing and micro-arc oxidation of TC4 alloy prepared based on SLM. *Mat. Chem. Phys.* 325, 129791. doi:10.1016/j.matchemphys.2024.129791

Xu, C., Peng, Y., Chen, L. Y., Zhang, T. Y., Cheng, J. J., and Wang, K. H. (2024b). Advanced cavitation erosion-corrosion resistance of nickel-aluminum bronze prepared by directed energy deposition. *Corros. Sci.* 231, 111982. doi:10.1016/j.corsci.2024.111982

Yang, P., Deng, Z., Chen, B., and Wang, Y. (2024). High-temperature dynamic corrosion mechanisms of austenitic stainless and carbon steels in nitrates for concentrating solar power. *Energy Mat. Sol. Cells* 266, 112690. doi:10.1016/j.solmat.2024.112690

Yu, W., Feng, Y., Guo, T., Wu, W., and Zhang, J. (2024). Insight into the Ni microalloying effects on the corrosion characteristics and mechanism of Fe-21Mn-10Al-1.25C lightweight steels in chloride-containing solution. *Constr. Build. Mat.* 456, 139313. doi:10.1016/j.conbuildmat.2024.139313

Zeng, D., Luo, J., Yu, C., Xiang, G., Mao, T., Wen, S., et al. (2025). Material selection of titanium alloy pipelines considering multi-criteria in an acidic environment based on analytic hierarchy process. *Int. J. Pres. Ves. Pip.* 216, 105461. doi:10.1016/j.ijpvp.2025.105461

Zhong, M., and Webler, B. A. (2024). High temperature oxidation behaviors of steels at initial stages in air. *Corros. Sci.* 229, 111838. doi:10.1016/j.corsci.2024.111838

Zhou, J., Tang, S., and Hu, J. (2025a). Oxide layer with excellent corrosion resistance obtained on carbon steel by pressure swing oxidation. *Surf. Sci.* 711, 164048. doi:10.1016/j.apsusc.2025.164048

Zhou, J., Ji, Y., Bai, H., Dong, X., Kang, X., and Li, Y. (2025b). Factors controlling evolution of nanoscale oxides in 316L stainless steel manufactured by powder bed fusion with laser beam. *Mat. Sci. Eng. A* 942, 148682. doi:10.1016/j.msea.2025.148682

Zhu, W., Zhang, Z. B., Yang, L., Zhou, Y. C., and Wei, Y. G. (2018). Spallation of thermal barrier coatings with real thermally grown oxide morphology under thermal stress. *Mat. Des.* 146, 180–193. doi:10.1016/j.matdes.2018.03.019